EVIDENCE FOR COMPOSITE HYDRAULIC ARCHITECTURE IN AN ACTIVE FAULT SYSTEM BASED ON 3D SEISMIC REFLECTION, TIME-DOMAIN ELECTROMAGNETICS AND TEMPERATURE DATA

Scott Hess[1], Jerry P. Fairley[2], John Bradford[1], Mitch Lyle[3], and William Clement[3]

ABSTRACT

Fault hydrology is a topic of scientific and practical importance, but considerable uncertainty exists regarding the nature of structural controls on fluid flow. Here we use seismic reflection and time-domain electromagnetic data to develop a three-dimensional model of hydraulic architecture in a predominantly dip-slip normal fault system, and we predict the architectural elements based on subsurface fluid flow patterns inferred from near-surface temperature measurements. Our observations indicate the presence of high-permeability flow paths parallel to fault planes in poorly-lithified sediments. These results are best explained using a combination of elements from commonly accepted conceptual models of fault architecture, a finding that exhibits the heterogeneous nature of the geologic materials comprising the site. These insights may be useful as a guide to future studies of active fault systems, where multiple-mode investigations (geophysical, hydrologic, thermal, geochemical) will be required to better understand subsurface fluid/fault interactions.

Keywords: fault hydrology, seismic reflection, TEM, geothermal systems, groundwater

INTRODUCTION

A great deal of work has been devoted to understanding various aspects of fault/fluid interactions (e.g., Talwani and Acree, 1985; Connolly and Cosgrove, 1999; Curewitz and Karson, 1997; Sibson, 2000). Monitoring of spring discharge and well data indicate that tectonic events influence groundwater chemistry and potentiometric distribution (e.g., Rojstaczer et al., 1995; Melchiorre et al., 1999; Akita and Matsumoto, 2004; Wang et al., 2004a, 2004b), and seismic activity has been linked to the spatial and temporal distribution of fault hydraulic properties (e.g., Talwani and Acree, 1985; Parotidis et al., 2004; Parotidis and Shapiro, 2004). The controls placed by faults on subsurface flow are important for understanding fault rheology (Byerlee, 1990; Rice, 1992) and the "heat flow paradox" (e.g., Zoback and Lachenbruch, 1992) of the San Andreas fault system, as well as having practical engineering and economic significance, for example, to the occurrence of ore bodies (e.g., Connolly and Cosgrove, 1999; Micklethwaite and Cox, 2004), petroleum migration and accumulation (e.g., Antonellini and Aydin, 1994, 1995), and the safe disposal of nuclear waste (Wittwer et al., 1995).

It is generally agreed that faults may act as a conduit for flow, a barrier to flow, or some combination of conduit/barrier, and a given fault may evolve over time to demonstrate any or all of these behaviors (Caine et al., 1996; Evans et al., 1997). Whether a particular fault acts as a conduit, a barrier, or is intermediate between these extremes is primarily a function of the morphology, or hydraulic architecture, of the fault, since individual architectural elements display characteristic permeability structures that collectively determine the behavior of subsurface fluids in the vicinity of the fault. A number of conceptual models of fault architecture have been proposed, the most widely

known of which are those of Antonellini and Aydin (1994, 1995), Caine et al. (1996), and Rawling et al. (2001); these models are believed to be applicable to faults in well-lithified sedimentary rocks, crystalline rocks, and alluvium or poorly-lithified sediments, respectively.

In a practical sense, it is seldom possible to determine the hydraulic architecture of an active fault in a field setting, since observations of the architectural elements in the subsurface are either indirect, or limited to a small area penetrated by a borehole or drift (e.g., Barton and Zoback, 1992; Barton et al., 1995; Shipton et al., 2002). Most studies of fault architecture, including those of Antonellini and Aydin (1994, 1995), Caine et al. (1996), and Rawling et al. (2001), are based on observations from exhumed, inactive faults, where surface exposures provide access to deformed materials for field or laboratory permeability studies (e.g., Rawling et al., 2001; Kato et al., 2004), textural studies (e.g., Chester and Logan, 1987; Evans and Chester, 1995; Steen and Andresen, 1999; Vermilye and Scholz, 1998, 1999; Evans and Bradbury, 2004), and field mapping of fractures and architectural elements (e.g., Jourde et al., 2002; Shipton and Cowie, 2001). As a result, studies of inactive faults have been indispensable for the evolution of conceptual models of fault/fluid interactions.

Recently, a number of investigators have used temperature measurements (e.g., Ge, 1998; Fairley et al., 2003; Bodvarsson et al., 2003) or temperature and hydrochemical data (e.g., Carreón-Diazconti et al., 2003; Fairley and Nicholson, 2006) to infer aquifer properties or subsurface flow fields, and these methods have been successfully applied to the problem of determining circulation patterns in active fault zones (e.g., Fairley and Hinds, 2004a). With increasing resolution, the potential for using surface-based thermal

methods to observe fault architectural elements *in-situ* has become more realistic, and attempts have been made to match field data from active faults with conceptual models of hydraulic architecture from the published literature (Fairley and Hinds, 2004a; Heffner and Fairley, 2006).

Unfortunately, surface-based thermal methods either provide depth-integrated information on fault properties (e.g., Fairley et al., 2003; Fairley and Hinds, 2004b) or are restricted to imaging processes in the shallow subsurface (e.g., Fairley and Hinds, 2004a; Fairley and Nicholson, 2006); therefore, additional data or analyses are required to obtain a true 3-dimensional view of fault architecture in an active system. Here we combine high-resolution seismic and time-domain electromagnetic (TEM) data with surface-based temperature data to characterize the hydraulic architecture of the fault-controlled Borax Lake Hydrothermal System (BLHS). Our goal is to integrate the geologic structure interpreted from the seismic and TEM data with the information on fluid flow provided by the near-surface temperature distribution, and to relate the resulting picture to models of fault architecture available in the published literature.

FAULT HYDRAULIC ARCHITECTURE

Because the three main conceptual models of fault hydraulic architecture (i.e., Antonellini and Aydin, 1994, 1995; Caine et al., 1996; Rawling et al., 2001) were developed for different geologic materials, they comprise complementary descriptions of the ways in which faults interact with subsurface fluids. Each of the conceptual models introduces unique architectural elements, although some features are shared by one or both alternative models. The main points of the three models are reviewed briefly below.

Faults in Well-Lithified Sedimentary Rocks

Antonellini and Aydin (1994, 1995) observed that faults in well-lithified sandstones are predominantly composed of three architectural elements, which they referred to as "deformation bands," "deformation band zones," and "slip surfaces." Because shearing associated with displacement results in crushing and a reduction of grain size, deformation bands and deformation band zones (DBZs) demonstrate a reduction in permeability in comparison to the undeformed protolith. Cataclasis arising from displacement associated with slip surfaces creates a barrier to flow normal to the plane of the fault, while providing high permeability pathways for concentrated flow parallel to the direction of displacement (Antonellini and Aydin, 1994, 1995).

Faults in Crystalline Rocks

A model of hydraulic architecture for faults in crystalline rocks comprises two main elements: a central, low-permeability core of gouge and cataclasite that accommodates most or all of the displacement across the fault, and flanking damage zones of brecciated, fractured, and otherwise deformed rock (Caine et al., 1996). By virtue of their ubiquitously fractured nature, damage zones are generally regarded as having intrinsically high permeability, and may form preferential pathways for fluid flow. Faults may act as barriers to flow, conduits, or combination conduit/barriers, and the architecture may be temporally variable, with the individual elements present in a fault zone changing as a function of offset, petrology, and other factors.

Faults in Poorly-Lithified Geologic Materials

The conceptual model for faults cutting alluvium and/or poorly lithified sediments developed by Rawling et al. (2001) includes deformation bands and DBZs, similar to the model of Antonellini and Aydin (1994, 1995) for well-lithified sedimentary rocks, but

introduces a new element, denoted as a "mixed zone," or area in which deformation had originally opened void spaces that were subsequently filled with unsorted debris. Mixed zones were found to be low in permeability, as a result of the compaction and wide range of clast sizes that are their defining characteristics. As a result, all the observed architectural elements were hypothesized by the investigators to lower permeability relative to the surrounding, undeformed sediments, and faults cutting poorly-lithified sediments were represented as barriers to flow.

SITE DESCRIPTION

The BLHS is located in the Pueblo Valley, in the southern part of the Alvord Basin in southeast Oregon (Figure 1). The Alvord Basin is a north trending graben, characteristic of the northern Basin and Range, bounded on the east and west sides by north trending normal faults (Pezzopane and Weldon, 1993; Blewitt et al., 2003) that show signs of recent activity (<2000 years bp; Hemphill-Haley, 1987). Displacements on these faults are 1,300 to 3,300 m along the range front of the High Steens and Pueblo Mountains to the west, and 350 to 1,300 m along the Trout Creek Mountains to the east (Cleary et al., 1981).

Basin fill in the vicinity of the BLHS consists of alluvial and lacustrine sediments, resting on siltstones and claystones that overlie Miocene volcanic rocks, including tuffs, basalts, and rhyolites (Fuller, 1931; Williams and Compton, 1953; Evans and Geisler, 2001). The depth of fill in the Alvord Basin is highly variable, in places reaching depths of close to 1000 m.

About 175 geothermal springs, linearly aligned in a roughly north-south orientation, mark the surface expression of the BLHS (Fairley and Hinds, 2004b). Spring

temperatures range from about 21 to 94 ºC (Fairley and Hinds, 2004b), and standard geothermometers indicate an approximate reservoir temperature of 200 – 250 ºC (Cummings et al., 1993; Koski and Wood, 2004). The pronounced surface expression of hydrothermal activity and linear trend of the hot springs imply active fault displacement since, when faults remain inactive for long periods of time, the high-permeability conduits transporting geothermal fluids become plugged with mineral precipitates (Curewitz and Karson, 1997). On the basis of gravity data, Cleary et al. (1981) hypothesized that the Borax Lake springs were controlled by a mid-basin normal fault, and Blackwell et al. (1986) proposed that a buried horst block was located in close proximity to the springs from examination of unpublished seismic reflection studies. These inferences of the subsurface structure are supported by more recent seismic reflection studies south of Borax Lake, that indicate a shallow (<100 m below land surface) mid-basin high, approximately aligned with the Borax Lake springs (Bradford et al., 2006). The available gravity and seismic data provide strong circumstantial evidence that geothermal discharge from the Borax Lake springs is fault controlled, and Bradford et al. (2006) concluded that the Borax Lake fault system is the most active system in the south end of the basin.

DATA COLLECTION

Data for the seismic, TEM, and temperature surveys described below were collected in an area centered on the left lateral step-over in the trend of the Borax Lake springs, which Fairley et al. (2003) used to divide the springs into the North and South Groups (Figure 2). Surface conditions range from dry, sparsely vegetated and poorly-developed soils west of the springs to wet precipitate and/or thick vegetation east of the springs,

with a maximum change in elevation of less than 3 m across the study area. There are 12 hot spring vents within the area of overlap of the seismic and temperature surveys, ranging in diameter from less than 0.5 m to approximately 2 m.

Temperature Survey

The temperature data were originally published in a study of the near-surface fault architecture by Fairley and Hinds (2004a), and are reinterpreted here to support the geophysical data gathered for the present study. A total of 800 ground and spring temperature measurements were collected in the 100 × 100 m survey area (Figure 2). Of the total 800 data points, 12 are averages of 3 to 5 measurements taken in each of the hot springs within the surveyed area. The remaining 788 are ground temperatures that were collected on a 5 × 5 m grid spacing; this spacing was reduced to 2.5 × 2.5 m in areas of rapid spatial variation in temperature. Ground temperatures were measured approximately 0.2 m below the land surface using handheld digital thermometers and heavy-duty thermocouple penetration probes, as described in Fairley and Hinds (2004a); ground temperatures are assumed to represent the near-surface fluids, given the shallow local water table. All data were collected during one day in May 2004, to minimize the influence of diurnal temperature fluctuations. Measured temperatures ranged from 12 to 89 ºC, with an average of 26 ºC (Figure 3).

Seismic Data Acquisition and Processing

From the surface expression of the hot springs, we expected the primary structures at the BLHS to be aligned in a roughly north–south orientation. However, the step over in the hot springs suggested that local three dimensional structural variability impacts the flow of fluids to the surface. With a primary objective of imaging these

structural controls in detail, we determined that full three-dimensional seismic data acquisition was necessary to image the structural architecture.

We conducted the seismic survey approximately 400 m north of Borax Lake, in the step-over area of the fault and centered on the line of hot springs (Figure 2). In order to optimally image offsets in stratigraphic layers due to faulting, we oriented the receiver and shot lines in an approximately east-west direction, perpendicular to the strike of the fault. The survey layout was designed to optimize shot-receiver offset and azimuthal coverage. The 240 channel receiver array consisted of eight lines with 30 receiver stations in each line (Figure 4). Inline receiver spacing was 5 m and crossline receiver spacing was 10 m. Source lines were parallel to receiver lines with inline spacing of 2.5 m, when coincident with receiver lines, and 5 m when between receiver lines. Spacing between source lines was 5 m. The source was a 7.62 mm semi-automatic rifle fired into 0.3 m deep, 3 cm diameter holes. The spread was rolled in the cross-line direction 10 times, with each spread having roughly 360 shot locations. The resulting average common-depth point fold, using a 2.5 m bin size, was 100+ over the target area. Sufficient offsets were needed to image bedrock outside of the noise cone, consisting primarily of airwave and ground roll energy (Baker et al., 1998), and to provide velocity control for normal moveout analysis. Detailed acquisition parameters for the seismic survey are given in Table 1.

Surface conditions in the area of the survey permitted fair to good source and receiver coupling; furthermore, elevation statics effects were negligible. We processed the seismic data using a typical processing flow (Table 2). Laterally variable zones of cemented sediment, open water, variable saturation, and unconsolidated material

produced a highly heterogeneous velocity structure in the very near surface (~0 – 2m depth). These conditions made the application of refraction and residual statics a critical step in the data processing flow. We manually picked over 8000 first break times to compute the refraction statics. For residual statics we used a modified form of the stack-power maximization algorithm described by Ronen and Claerbout (1985), where a pilot trace is cross-correlated with each trace in the active CMP to determine the time shifts that maximize the stack-power within some time gate. This method is surface-consistent, implying that the time correction depends only on the surface location of the shot and receiver associated with the trace. The statics processing sequence substantially improved prestack reflector coherence (Figure 5) thereby improving velocity analysis and the final stack result (Figure 6). Stacking velocities ranged from 1400 for the shallowest reflectors to 2000 m/s at around 150 ms, and showed little lateral variation. This result indicates that velocity heterogeneity associated with the hot springs and faulting was below the resolution of CMP velocity analysis, and therefore occurred at a length scale substantially smaller than a receiver spread length. We conclude that the velocity model derived from CMP analysis cannot be used directly to image the fault system in this case.

We interpreted horizons in the seismic volume using a semiautomated algorithm that located the common phase along reflectors that were initially picked visually. Fault positions were interpreted visually along each east-west profile, then interpolated in the north-south direction with a best fit line display purposes.

Time-domain electromagnetics

To further constrain our interpretation of the system we acquired two orthogonal time-domain electromagnetic (TEM) profiles within the 3-D seismic survey area (Figure

2). The survey consisted of deploying two horizontal co-planar loops; a 20 x 20 m square transmitter loop and a 5 x 5 m square receiver loop, resulting in a 25 m^2 dipole moment. The receiver loop was placed at the center of the transmitter loop. We recorded 31 time windows, from approximately 1 μs to about 3 ms, using a Zonge GDP-16. A Zonge NanoTEM NT-20 transmitter supplied an input current of about 3.7 A for all the collected data. We used the recommended recording parameters for a 20 x 20 m transmitter loop; a 50 % duty cycle, a 1.5 μs transmitter (Tx) delay, a 2.0 μs receiver (Rx) delay, and the antialias filter was on. Using this configuration, the turnoff time was 1.5 μs, and 1024 samples were collected for each data window. We used the 6.94 μs window to monitor the field noise. Using the standard error of the mean (SEM), the estimated data error for that window was less than 0.1%. Since we stacked the data in the field, we only have an error estimate for this time window. The transmitter loop was moved 15 meters to provide 5 m overlap with the proceeding loop, so that the surface was covered continuously in the survey region. An example decay curve is shown in Figure 7.

We inverted the data using INTERPEX's TEMIX XL software package. For each central loop array, we removed the time windows greater than 1.5 ms before inverting the data. These time windows were too noisy to provide reliable data for the inversions. We then used the smooth inversion option within TEMIX XL to determine the 1-dimensional resistivity structure below each measurement location. In TEMIX XL, the smooth inversion uses constant thickness layers, then we allow the inversion to determine the resistivities. We use the default values provided by TEMIX XL for the inversion which include 15 layers, less than 20 iterations, and convergence is achieved when the RMS deviation is less than 1% or when the deviation changes by less than 3%. The inversion

uses a ridge regression algorithm to provide the best fit to the data in a least squares sense (Inman, 1975).

The 1-D inversion results provide a relatively detailed picture of the resistivity structure at the BLHS. We display the combined 1-D inversions in Figure 8. While each TEM sounding was inverted independently, the resulting profiles are laterally consistent with the main layering and anomalies varying gradually along the profiles. This consistency provides a level of confidence in the validity of the results. Note that we applied a gentle smoothing operator for plotting which removes the sharp lateral boundaries due to minor differences in the inversions resulting in a more easily interpreted depth section.

RESULTS

There are three main features evident in the seismic data cube that we will focus on for the remainder of the discussion. The first is the strongest and most continuous reflection (R_B) which has a traveltime of ~135 ms in the southern part of the survey area and dips gently northward to a maximum traveltime of 175 ms in the north (Figure 6). . The traveltimes correspond to depths of 120 and 156 m respectively. R_B is continuous throughout the western 75% of the survey area but is truncated abruptly along a linear trend that is east of, and sub-parallel to, the south hot springs groups. We interpret this truncation as coinciding with the second major feature; the eastward dipping Borax Lake normal fault (BLF). Cross-sections through the data volume show semi-continuous reflections overlying the R_B horizon that are not terminated by the BLF, but have decreased continuity and amplitude, indicative of fault-related deformation (Figure 6). The reflector R_B is planar and dips gently toward the west in the south half of the study

area but changes character substantially toward the north. North of the hot springs stepover, the western section of R_B rotates downward to the east and is offset from the central portion of the horizon (Figure 6). A time slice through the stack volume shows that steeply dipping and irregular areas of R_B associated with this offset follow a linear trend that aligns with the trend of the hot springs (Figure 9). This change in character indicates the onset of the third major feature: a west-dipping normal fault (WF) that first appears at the step over in the hot springs (Figures 6). By examining a contour map of the R_B surface, we find that offset along the WF gradually increases towards the northern boundary of the seismic study area where it reaches a maximum of roughly 10 m (Figure 10). Zones of low seismic amplitude along R_B probably indicate fault damage zones where acoustic impedance boundaries are irregular due to fracturing. Projecting the faults from depth (Figure 10) to the surface as in Figure 6, we find that the BLF roughly corresponds to the south group of hot springs, while the WF projection approximately corresponds to the north group.

The TEM profiles reveal a relatively detailed picture of the shallow resistivity structure with laterally coherent layering and subvertically oriented anomalies that are likely associated with geothermal fluid distribution along the fault zones (Figure 8). The profiles show high resistivity at the surface to depths of about 6 m along both the east-west and north-south lines. This surface layer is underlain by a 1 to 2 m thick low resistivity layer. These two layers roughly parallel the surface topography.

In the east-west line, steeply dipping low resistivity features occur between 1225 and 1200 m elevation. These features merge near the surface beneath the hot springs groups, and their trend is consistent with the WF and BLF fault seismic interpretations. Centered

at about 1210 m elevation, a relative high resistivity zone is present between the two hot springs groups.

In the north-south profile, the top of a 4-5 m thick low resistivity anomaly is seen dipping toward the north from an elevation of 1225 m in the south to 1220 m at the northern end. This sturcture follows the dip of the bedrock interface in our seismic interpretation, but the feature is much shallower.

The near-surface temperature data plotted in Figure 3 show two ridges of elevated temperature, coincident with the two lines of hot springs visible at the surface. The data of Figure 3 are consistent with the findings of Fairley and Hinds (2004a), who interpreted the regions of elevated temperature as resulting from geothermal fluids, rising along structurally-controlled pathways. This general interpretation is supported by the seismic data. The temperature ridges indicate higher temperature, near-surface geothermal fluid, and the locations of these ridges coincide closely with the surface projections of the BLF (east) and WF (west) faults interpreted from the seismic volume. Both the data of Fairley and Hinds (2004a) and that shown in Figure 3 indicate the discharging fluids gradually cool and migrate north and east of the springs, and this interpretation is supported by the local vegetation pattern.

DISCUSSION

The extensive precipitate deposits in the area of the BLHS and bedrock outcrops 1 km south of Borax Lake influenced previous investigators to estimate the depth to bedrock to be on the order of 5 m (e.g. Fairley and Hinds, 2004a). However, the seismic data we present here shows a strong reflector much deeper and the measured seismic velocities at such shallow depths are too slow to be lithified rock. Based on comparisons

to the stratigraphy in two wells drilled about 2-4 km to the south and outcropping sedimentary rock, a plausible geologic interpretation for the stratigraphy observed in the seismic data is that the reflector R_B indicates the top of a well-lithified sedimentary unit dipping gently to the northwest, overlain by layers of moderately- or poorly-lithified alluvium and lacustrine sediments. We interpret the east-dipping BLF fault as the northward extension of the east-bounding fault of the mid-basin basement high imaged by Bradford et al. (2006). Since we do not image reflectors below R_B east of the BLF in our 3D seismic data, we cannot determine the offset of the BLF in this area, but it could be as much as 400 m or more (Bradford et al., 2006). Evidence for a complementary west bounding fault for the mid-basin has been interpreted in gravity data by Cleary et al. (1981). The west-dipping fault, WF, from the 3-D seismic data has insufficient offset to form the corresponding west boundary of the basement high, but is an eastern branch of a larger fault that may lie as much as 300 - 400 m west of the BLF based on projections from unpublished seismic data located to the south.

The TEM interpretations corroborate the seismic reflection results and are consistent with the temperature measurements. Strike perpendicular east-west profiles show two steeply dipping low resistivity zones converging below the step-over in the hot springs (Figure 8). These low resistivity zones are roughly aligned with the WF and BLF faults from our seismic interpretation (Figure 11). These TEM results support the interpretation of two oppositely dipping faults converging at the surface. There are many possible interpretations of the low resistivity anomalies (changes in salinity, increased clay content etc.). However, the surface projection of the low resistivity anomalies corresponds to high temperature anomalies and given the geometry of the resistivity structures and that

the system is well mixed due to circulation of the geothermal fluids, we believe that the most likely explanation is an increase in water content associated with an increase in pore space along the fracture zones. However, it is likely that temperature contributes to the observed resistivity anomalies, given the large thermal variation between vents (Figure 3).

A simplistic approach to categorizing fault architecture would be to assign the BLF a low effective permeability value as predicted by the Rawling et al. (2001) model since, according to the 3-D seismic data, the fault displaces alluvium and valley fill deposits that are approximately 140 m thick. It is clear from an examination of the temperature data shown in Figure 3, however, that hydrothermal fluids are moving up-dip along structurally-controlled pathways associated with the BLF, and perhaps by fault WF. Since the Rawling et al. (2001) model does not allow for the formation of preferential, high-permeability flow paths associated with fault deformation, an alternative model is required to explain the behavior of the BLHS. We propose that a hybrid of the three standard conceptual models best fits the observations of the Borax Lake system, on the basis of a detailed examination of the seismic survey results and the near-surface temperature data.

Although the geophysical survey results do not allow the source of the upwelling geothermal fluids to be identified, an artesian well drilled as part of a sodium prospecting project during the late 1950s or early 1960s (Schneider and McFarland, 1995) and exploration wells drilled by Anadarko Production Company in the early 1990s (Blackwell et al., 1986) all encountered geothermal fluids to the east and/or southeast of the BLF; to the best of our knowledge, all recorded wells west of the BLF are of ambient,

or at most only slightly elevated temperatures (Schneider and McFarland, 1995). Lithological logs for the Anadarko boreholes indicate thermal fluids are migrating laterally from east to west, along flow paths constrained above and below by zones of fractures sealed with calcite and silica precipitates, similar to the model proposed by Healy and Hochstein (1973). We hypothesize that this lateral flow of hydrothermal fluids intersects the BLF at depth, and that the BLF forms the primary conduit controlling the migration of these fluids towards the surface.

Regardless of the mechanism by which geothermal fluids are introduced to the BLF at depth, the linear, narrowly-focused distribution of springs and elevated temperatures at the land surface (Figure 3), and the correlation between areas of elevated temperatures and apparent fault-related displacement suggest the presence of high-permeability flow paths associated with, and parallel to, the BLF (Figures 6, 8, and 11). Previous investigators attributed the distribution of upwelling geothermal fluids to high-permeability damage zones flanking a low-permeability core of the BLF (Fairley and Hinds, 2004a); however, this explanation cannot be confirmed on the basis of the geophysical data. It is equally probable that the observed distribution of pathways is the result of flow along high-permeability slip surfaces, as described by the Antonellini and Aydin (1994, 1995) model. In either case, the presence of interconnected, spatially-correlated voids is required to explain the observed pattern of discharge. Similar to Heffner and Fairley (2006), we hypothesize that extensive precipitation of amorphous silica from upwelling geothermal fluids cements the near-surface basin fill in the vicinity of the BLF, causing the sediments to behave similar to well-lithified materials, and allowing open fractures and/or slip surfaces to form. This conjecture is supported by the

extensive deposits of precipitate found in close association with the trace of the BLF, and the rapid decline in the density of precipitate with increasing distance from the surface expression of the fault.

Although the BLF probably exerts primary structural control on vertical migration of geothermal fluids, the WF apparently forms an important part of the near-surface hydraulic architecture of the BLHS. An examination of the seismic cross-sections from south to north shows that the first appearance of the WF coincides with the left-step that divides the South Group springs from the North Group springs (Figure 6). WF increases in offset toward the north, and is continuous to the northern boundary of the study area. Furthermore, the projection of fault WF to the land surface corresponds with the western edge of the North Group temperature anomaly (Figure 11). Fairley and Hinds (2004a) suggest the presence of a low-permeability fault core in this region, blocking the lateral movement of shallow discharge to the west. The data presented here are consistent with the idea of a low-permeability barrier to flow in this area; however, the apparent offset across WF, particularly in the area of the step-over, is probably insufficient for the development of an appreciable fault core. We therefore deviate from the conceptual model of Heffner and Fairley (2006) in proposing that displacement across fault WF resulted in the development of a low-permeability mixed zone similar to those described in the Sand Hill fault by Rawling et al. (2001). The seismic and thermal data are equally consistent with the development of DBZs local to WF, but the obvious surficial precipitate deposits found near the springs terminate 10 – 20 m east of the projected trace of WF. Without the rigidity imparted to the surface sediments by extensive mineral

precipitation, it appears doubtful that narrow, focused bands of deformation such as those described by Antonellini and Aydin (1994, 1995) could develop.

Although alternative genetic explanations exist for each of the architectural elements of the BLHS, the role of barrier or conduit for each element is made clear by the combined seismic, TEM, and thermal data. A schematic representation of the hydraulic architecture of the BLHS that incorporates the main points discussed above is presented in Figure 12.

CONCLUSIONS

We use a combination of high-resolution, near-surface temperature measurements and geophysical data to examine the hydraulic architecture of the Borax Lake Hydrothermal System in the Alvord Basin of southeast Oregon. Our investigation reveals the presence of a previously unknown, westward-dipping fault of relatively small offset, in addition to the east-dipping Borax Lake normal fault. The faults play significant and distinct roles in determining the subsurface flow of geothermal fluids, and the control exerted by each fault is probably strongly influenced by the presence or absence of precipitation associated with geothermal discharge.

The seismic, TEM, and temperature data from the BLHS are probably best interpreted using a combination of architectural elements taken from published conceptual models of hydraulic architecture. Such a "composite" model allows the flexibility to incorporate insights from a variety of systems to account for highly heterogeneous subsurface conditions; in the Borax Lake system, for example, these include areas of alluvium and weakly-lithified sediments, zones of well-cemented sediments that act similar to well-lithified rocks, and well-lithified sedimentary bedrock

at depth. In the future, we hope studies of active fault systems combining geophysical methods, temperature data, borehole-based testing and other tools will clarify the architectural elements of influencing fault hydrology, and provide a greater understanding of the relationships between structural/mechanical deformation, geologic materials, and subsurface fluid flow.

ACKNOWLEDGEMENTS

The authors would like to thank J. Hinds, T. Anderson, A. Colter, C. Opatz, N. Whitaker, and J. Zakrajsek for assistance with temperature data collection. Idaho/EPSCoR and the National Science Foundation (award EPS-0132626) funded this work.

REFERENCES

Akita, F., and N. Matsumoto, 2004. Hydrological responses induced by the Tokachi-oki earthquake in 2003 at hot spring wells in Hokkaido, Japan: Geophysical Research Letters **31**, L16603, doi:10.1029/2004GL020433.

Antonellini, M., and A. Aydin, 1994. Effect of faulting on fluid flow in porous sandstones. Petrophysical properties. American Association of Petroleum Geologists Bulletin **78**, 355-377.

Antonellini, M., and A. Aydin, 1995. Effect of faulting on fluid flow in porous sandstones: Geometry and spatial distribution. American Association of Petroleum Geologists Bulletin **79,** 642-671.

Baker, G.S., D.W. Steeples, and M. Drake, 1998. Muting the noise cone in near-surface reflection data: An example from southeastern Kansas. Geophysics **63**, 1332-1338.

Barton, C.A., and M.D. Zoback, 1992. Self-similar distribution and properties of macroscopic fractures at depth in crystalline rock in the Cajon Pass Scientific Drill Hole. Journal of Geophysical Research **97**, 5181-5200.

Barton, C.A., M.D. Zoback, and D. Moos, 1995. Fluid flow along potentially active faults in crystalline rock. Geology **23**, 683-686.

Blackwell, D.D., S.A. Kelley, and R.C. Edminston, 1986. Analysis and interpretation of thermal data from the Borax Lake geothermal prospect, Oregon. Geothermal Resources Council Transactions **10**,169-174.

Blewitt, G., M. Coolbaugh, D. Sawatzky, W. Holt, J. Davis, and R. Bennett, 2003. Targeting of potential geothermal resources in the Great Basin from regional to basin-scale relationships between geodetic strain and geological structures. Proceedings, Annual GRC Meeting, Morelia, Mexico, October 12-15, 2003: Davis, California, Geothermal Resources Council Transactions **27**, 3-7.

Bodvarsson, G.S., E. Kwicklis, C. Shan, and Y.S. Wu, 2003. Estimation of percolation flux from borehole termperature data at Yucca Mountain, Nevada. Journal of Contaminant Hydrology **62 – 63**, 3-22.

Bradford, J.H., L. Liberty, M. Lyle, B. Clement, and S. Hess, 2006. Imaging complex structure in shallow seismic-reflection data using pre-stack depth migration. Geophysics **71**, B175-B181.

Byerlee, J., 1990. Friction, overpressure and fault normal compression. Geophysical Research Letters **17**, 2109-2112.

Caine, J.S., J.P. Evans, and C.B. Forster, 1996. Fault zone architecture and permeability structure. Geology **24**, 1025-1028.

Carreón-Diazconti, C., S.T. Nelson, A.L. Mayo, D.G. Tingey, and M. Smith, 2003. A mixed groundwater system at Midway, UT: Discriminating superimposed local and regional discharge. Journal of Hydrology **273**, 119-138.

Chester, F.M., and J.M. Logan, 1987. Composite planar fabric of gouge from the Punchbowl Fault, California. Journal of Structural Geology **9**, 621-634.

Cleary, J., I.M. Lange, A.I. Qamar, and H.R. Krouse, 1981. Gravity, isotope, and geochemical study of the Alvord Valley geothermal area, Oregon. Geological Society of America Bulletin, Part II **92**, 934-962.

Connolly, P., and J. Cosgrove, 1999. Prediction of static and dynamic fluid pathways within and around dilational jogs. Fractures, Fluid Flow and Mineralization, K.J.W. McCaffrey, L. Lonergan, and J.J. Wilkinson, editors. Geological Society of London, Special Publications **155**, 105-121.

Cummings, M.L., A.M. St. John, and N.C. Sturchio, 1993. Hydrogeochemical characterization of the Alvord Basin geothermal area, Harney County, Oregon, USA. Proceedings of the 15th New Zealand Workshop, Auckland, New Zealand, 119-124.

Curewitz, D., and J.A. Karson, 1997. Structural settings of hydrothermal outflow: Fracture permeability maintained by fault propagation and interaction. Journal of Volcanology and Geothermal Research **79**, 149-168.

Evans, J.G., and T.M. Geisler, 2001. Geologic Field-Trip Guide to Steens Mountain Loop Road, Harney County, Oregon. U.S. Geological Society and U.S. Department of the Interior.

Evans, J.P., and F.M. Chester, 1995. Fluid-rock interaction in faults of the San Andreas system: Inferences from San Gabriel fault rock geochemistry and microstructures. Journal of Geophysical Research **100(B7)**, 007-13,020.

Evans, J.P., C.B. Forster, and J.V. Goddard, 1997. Permeability of fault-related rocks, and implications for hydraulic structure of fault zones. Journal of Structural Geology **19**, 1393-1404.

Evans, J.P., and K.K. Bradbury, 2004. Faulting and fracturing of nonwelded Bishop Tuff, Eastern California: Deformation mechanisms in very porous materials in the Vadose Zone. Vadose Zone Journal **3**, 602-623.

Fairley, J.P., J. Heffner, and J.J. Hinds, 2003. Geostatistical evaluation of permeability in an active fault zone, Geophysical Research Letters **30**, 1962, doe:10.1029/2003GL018064.

Fairley, J.P., and J.J. Hinds, 2004a. Field observation of fluid circulation patterns in a normal fault system. Geophysical Research Letters **31**, L19502, doi:10.1029/2004GL020812.

Fairley, J.P., and J.J. Hinds, 2004b. Rapid transport pathways for geothermal fluids in an active Great Basin fault zone. Geology **32**, 825-828.

Fairley, J.P., and K.N. Nicholson, 2006. Imaging lateral groundwater flow in the shallow subsurface using stochastic temperature fields. Journal of Hydrology **321**, 276 -285.

Fuller, R.E., 1931. The Geomorphology and Volcanic Sequence of Steens Mountain in Southeastern Oregon. University of Washington Publication in Geology **3**, 1-130. University of Washington Press, Seattle, Washington.

Ge, S., 1998. Estimation of groundwater velocity in localized fracture zones from well temperature profiles. Journal of Volcanology and Geothermal Research **84**, 93-101.

Healy, J., and M.P. Hochstein, 1973. Horizontal flow in hydrothermal systems. Journal of Hydrology, New Zealand **12**, 71-82.

Hemphill-Haley, M.A., 1987. Quaternary Stratigraphy and Late Holocene Faulting Along the Base of the Eastern Escarpment of Steens Mountain, Southeastern Oregon. M.A. thesis, Humboldt State University , Arcata, California, 87 pp.

Heffner, J., and J.P. Fairley, 2006. Using surface characteristics to infer the permeability structure of an active fault zone. Journal of Sedimentary Geology **184**, 255-265.

Inman, J.R., 1975, Resistivity inversion with ridge regression. Geophysics **40**, 798-817.

Jourde, H., E.A. Flodin, A. Aydin, L.J. Durlofsky, and X.H. Wen, 2002. Computing permeability of fault zones in eolian sandstone from outcrop measurements. American Association of Petroleum Geologists Bulletin **86**, 1187-1200.

Kato, A., A. Sakaguchi, S. Yoshida, H. Yamaguchi, and Y. Kaneda, 2004. Permeability structure around an ancient exhumed subduction-zone fault. Geophysical Research Letters **31**, L06602, doi:10.1029/2003GL019183.

Koski, A.K., and S.A. Wood, 2004. The geochemistry of geothermal waters in the Alvord Basin, southeastern Oregon. Proceedings of the 11th International Symposium on Water-Rock Interaction, WRI-11, Saratoga Springs, NY, 149-152.

Melchiorre, E.B., R.E. Criss, and M.L. Davisson, 1999. Relationship between seismicity and subsurface fluids, central Coast Ranges, California. Journal of Geophysical Research **104**, 921-939.

Micklethwaite, S., and S.F. Cox, 2004. Fault-segment rupture, aftershock-zone fluid flow, and mineralization. Geology **32**, 813-816.

Parotidis, M., and S.A. Shapiro, 2004. A statistical model for the seismicity rate of fluid-injection-induced earthquakes, Geophysical Research Letters **31**, L17609, doi: 10.1029/2004GL020421.

Parotidis, M., S.A. Shapiro, and E. Rothert, 2004. Back front of seismicity induced after termination of borehole fluid injection, Geophysical Research Letters **31**, L02612, doi:1029/2003GL018987.

Pezzopane, S.K., and R.J. Weldon, 1993. Tectonic role of active faulting in Central Oregon. Tectonics **12**, 1140-1169.

Rawling, G.C., L.B. Goodwin, and J.L. Wilson, 2001. Internal architecture, permeability structure, and hydrologic significance of contrasting fault-zone types. Geology **29**, 43-46.

Rice, J.R., 1992. Fault stress states, pore pressure distributions, and the weakness of the San Andreas Fault. Fault Mechanics and Transport Properties of Rocks, B. Evans and T.F. Wong, editors, pp. 475-503, Academic Press, San Diego, California.

Rojstaczer, S., S. Wolf, and R. Michel, 1995. Permeability enhancement in the shallow crust as a cause of earthquake-induced hydrological changes. Nature **373**, 237-239.

Ronen, J., and J.F. Claerbout, 1985. Surface-consistent residual statics estimation by stack-power maximization. Geophysics **50**, 2759-2767.

Schneider, T.R., and W.D. McFarland, 1995. Hydrologic Data and Description of a Hydrology Monitoring Plan for the Borax Lake Area, Oregon. U.S. Geological

Survey Open-File Report 95-367, U.S. Geological Survey, Portland, Oregon, 24 pages.

Shipton, Z.K., and P.A. Cowie, 2001. Damage zone and slip-surface evolution over μm to km scales in high-porosity Navajo sandstone, Utah. Journal of Structural Geology **23**, 1825-1844.

Shipton, Z.K., J.P. Evans, S.R. Robeson, C.B. Forster, and S. Snelgrove, 2002. Structural heterogeneity and permeability in faulted eolian sandstone: Implications for subsurface modeling of faults. American Association of Petroleum Geologists Bulletin **86**, 863-883.

Sibson, R.H., 2000. Fluid involvement in normal faulting. Journal of Geodynamics **29**, 469-499.

Steen, Ø., and A. Andresen, 1999. Effects of lithology on geometry and scaling of small faults in Triassic sandstones, East Greenland. Journal of Structural Geology **21**, 1351-1368.

Talwani, P., and S. Acree, 1985. Pore pressure diffusion and the mechanism of reservoir-induced seismicity. Pure and Applied Geophysics **122**, 947-965.

Vermilye, J.M., and C.H. Scholz, 1998. The process zone: A microstructural view of fault growth. Journal of Geophysical Research **103**, 12,223-12,237.

Vermilye, J.M., and C.H. Scholz, 1999. Fault propagation and segmentation: insight from the microstructural examination of a small fault. Journal of Structural Geology **21**, 1623-1636.

Wang, C.Y., M. Manga, D. Dreger, and A. Wong, 2004a. Streamflow increase due to rupturing of hydrothermal reservoirs: Evidence from the 2003 San Simeon,

California, earthquake. Geophysical Research Letters **31**, L10502, doi:1029/2004GL020124.

Wang, C.Y., C.H. Wang, and M. Manga, 2004b. Coseismic release of water from mountains: Evidence from the 1999 (M_w = 7.5) Chi-Chi, Taiwan, earthquake. Geology **32**, 769-772.

Williams, H., and R.R. Compton, 1953. Quicksilver Deposits of Steens Mountain and the Pueblo Mountains, Southeast Oregon. U.S. Geological Survey Bulletin 995-B.

Wittwer, C., G.S. Bodvarsson, E. Kwicklis, A. Flint, and G. Chen, 1995. Preliminary Development of the LBL/USGS Three-Dimensional Site-Scale Model of Yucca Mountain, Nevada. LBL Report LBL-37356, Lawrence Berkeley National Laboratory, California.

Zoback, M.D., and A.H. Lachenbruch, 1992. Introduction to special section on the Cajon Pass Scientific Drilling Project. Journal of Geophysical Research **97**, 4991-4994.

TABLE CAPTIONS

Table 1: Seismic survey acquisition parameters.

Table 2. Processing flow for seismic data.

FIGURE CAPTIONS

Figure 1: Shaded relief map showing the location of the Borax Lake Hydrothermal System in the Alvord Basin of southeast Oregon (from Heffner and Fairley, 2006).

Figure 2: Map showing the relative locations of the thermal survey and TEM (blue crosses) profiles with respect to the seismic survey and the hot spring locations (red dots). Black dashed lines show location of seismic cross sections discussed in the text.

Figure 3: Shaded contour map of ground and spring temperatures. Hot spring vents located in the study area are indicated by the triangles.

Figure 4. Schematic of the 3D seismic survey. This receiver spread pattern was rolled approximately 200 meters in the cross-line direction at 20 meter intervals.

Figure 5. Shot gathers with AGC and bandpass filter applied exhibit a large noise cone and two main reflection packages around 100 and 150 ms. Before the application of refraction and residual statics (top), the gathers have small undulations along the first arrivals and reflections, while the gathers after refraction and residual statics (bottom) have smooth and more coherent first arrivals and reflections. Notice that each receiver line has noticeable improvement, and some have quite significant improvement such as channels 150 – 180.

Figure 6. Two cross-line slices illustrate how R_B (yellow) changes from south (B) to north (A) and shows the relative location of the faults (red) with respect to the hot springs. Two in-line slices show R_B in between (C) and to the west (D) of the north

group (NG) and south group (SG) of hot springs. The decreased continuity and amplitude of the shallow reflectors in profile C compared to profile D indicates the effects of the converging faults. The locations of these cross-sections are shown in the bottom right corner. (V.E. ~ 2:1)

Figure 7. Example TEM decay curve. The record was truncated at 27 samples for inversion.

Figure 8. Cross structure (west-east) and along structure (south-north) TEM profiles collected at the BLHS show conductive zones that are likely associated with geothermal water and increased temperature (see Figure 2 for locations). The resistive layer at the surface corresponds to the vadose zone. The dashed lines are the interpreted locations of WF and BLF from the seismic data. The arrows indicate where the profile crosses each group of hot springs. Intersection of the two profiles are indicated with a dotted line. The vertical exaggeration on both profiles is approximately 4:1.

Figure 9. A time slice at 160 ms two-way traveltime through the seismic volume clearly shows linear events that are subparallel to the trend of the hot springs. These high spatial frequency linear features occur where the constant time slice intersects topographic irregularities in R_B.

Figure 10. Contouring the R_B traveltime horizon illustrates that WF increases in offset toward the north and how the orientations of the WF and BLF match the surface trend of the hot springs (triangles). The fault positions shown here correspond to the location of R_B faulting at the depth of the horizon. Projecting the faults to the surface as in Figure 6, we find that the WF corresponds to the north group of hot springs while the BLF corresponds to the south group of hot springs.

Figure 11. Coincident east-west TEM slice, seismic section, and temperature profile shows that the converging high conductivity zones and high temperatures correlate well with two oppositely dipping faults converging at the surface.

Figure 12. Schematic representation of hydraulic architecture in the step-over area of the Borax Lake fault zone. Arrows represent flow paths for geothermal fluids rising up the Borax Lake fault, and discharging through springs and as lateral flow through the near-surface sediments. The numbers indicate hypothesized architectural elements associated with near-surface faulting: 1) zones of deformation banding and slip-slip surfaces, formed in sediments cemented by precipitates associated with geothermal discharge; 2) low-permeability mixed zone or deformation banding resulting from offset on fault WF, and forming a barrier to westward fluid migration; 3) damage zone and/or deformation banding and slip-surface development at the interface between bedrock (on the up-thrown block) and juxtaposed sediments (overlying the down-thrown block) across the Borax Lake fault.

Table 1. Hess

- 7.62x39 mm SKS rifle source w/ blast shield - 240 channel recording system - 40 Hz single geophones - 750 ms recording time - 2 vertical stack - 5 m and 2.5 m in-line source interval - 5 m cross-line source interval - 5 m in-line receiver interval - 10 m cross-line receiver interval - 240 m maximum offset - 25 Hz low-cut filter - 20 m roll in cross-line direction

Table 2. Hess

- Preprocessing - Trace Mutes - Bandpass Filter (30-60-200-400) Hz - AGC (80 ms time gate) - Semblance Velocity Analysis - Refraction / Residual Statics - Semblance Velocity Analysis - Normal Moveout Correction - Common Mid-Point Stacking - 3-D Coherence Filter (3 trace mix)

Figure 1. Hess

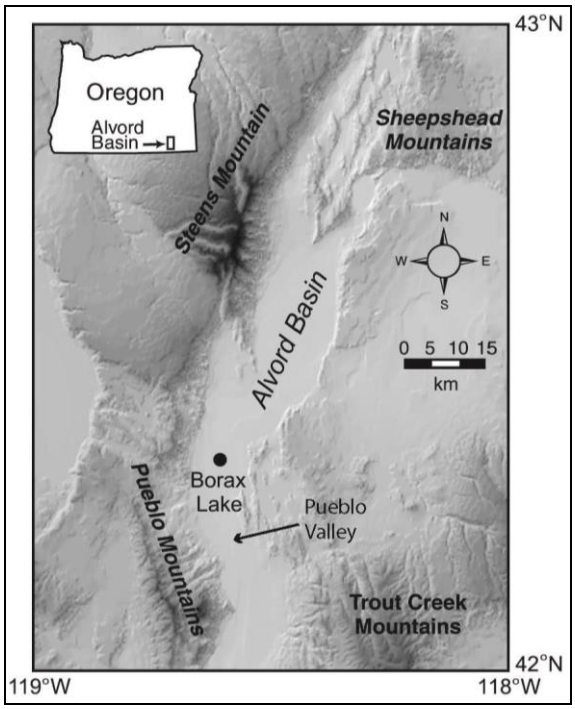

Figure 2. Hess

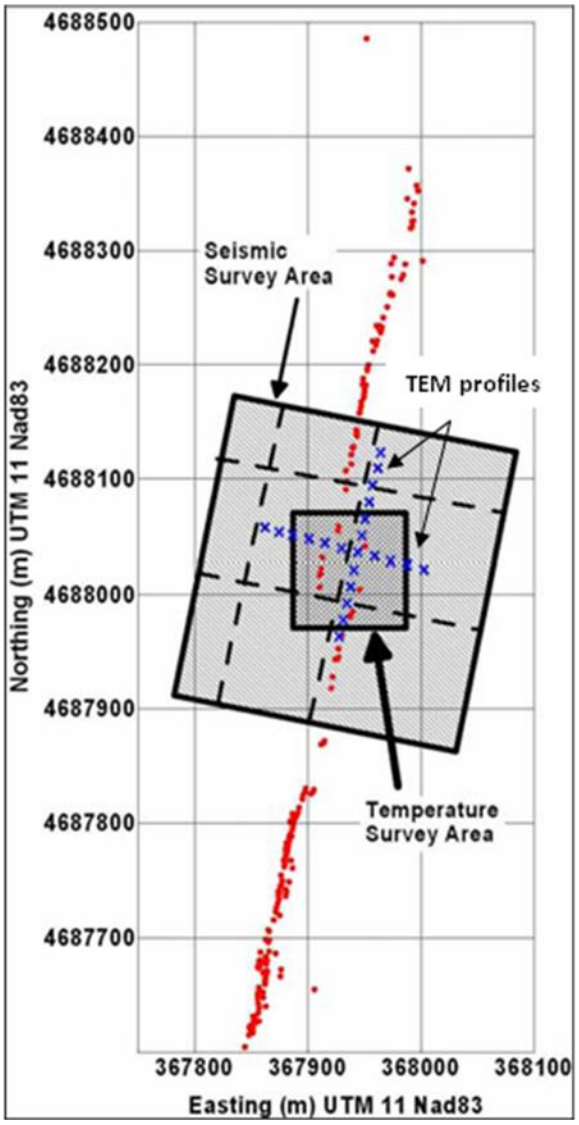

Figure 3. Hess

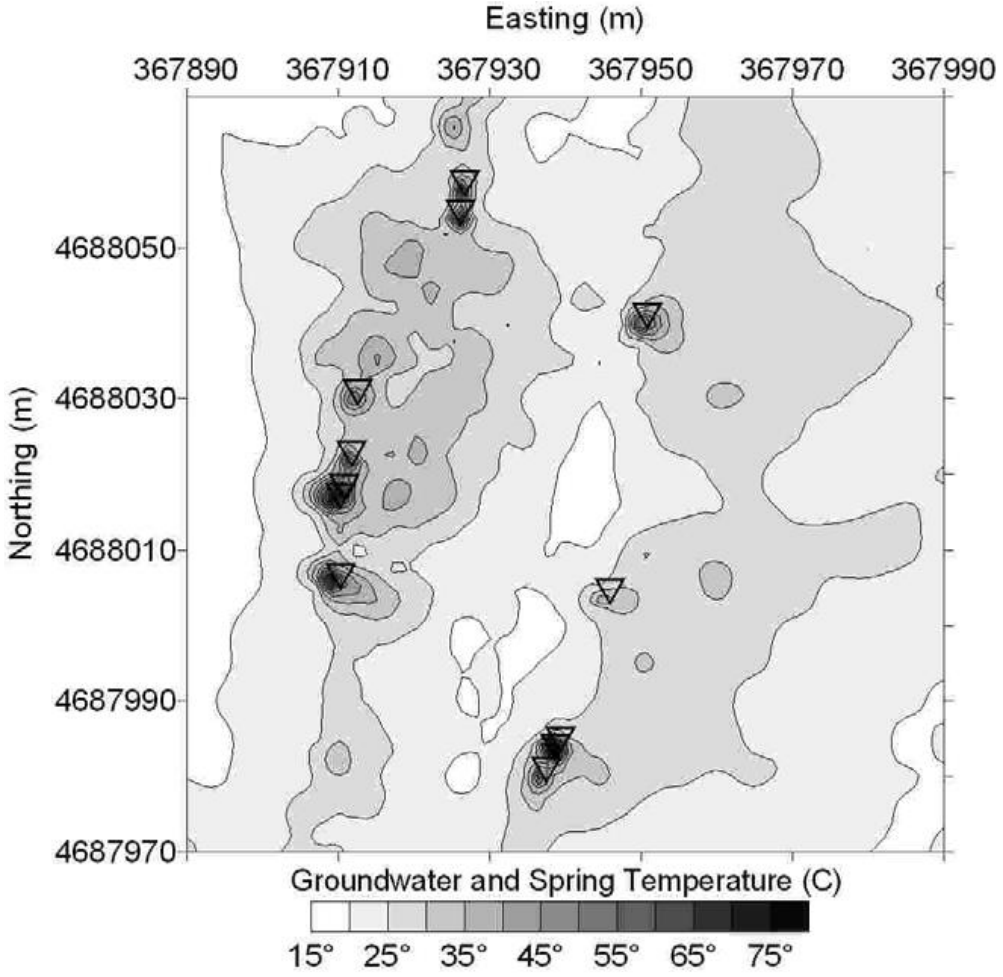

Figure 4. Hess

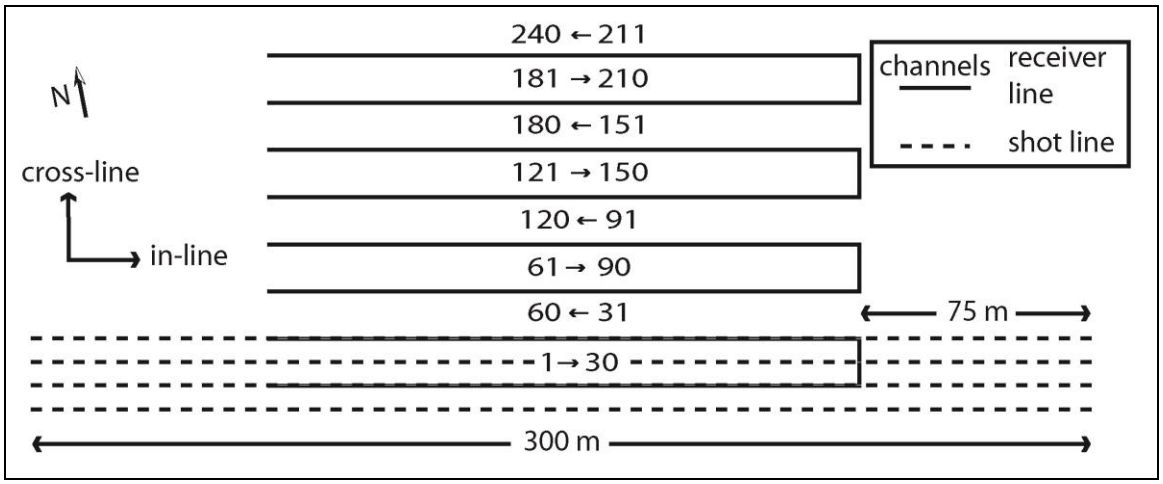

Figure 5. Hess

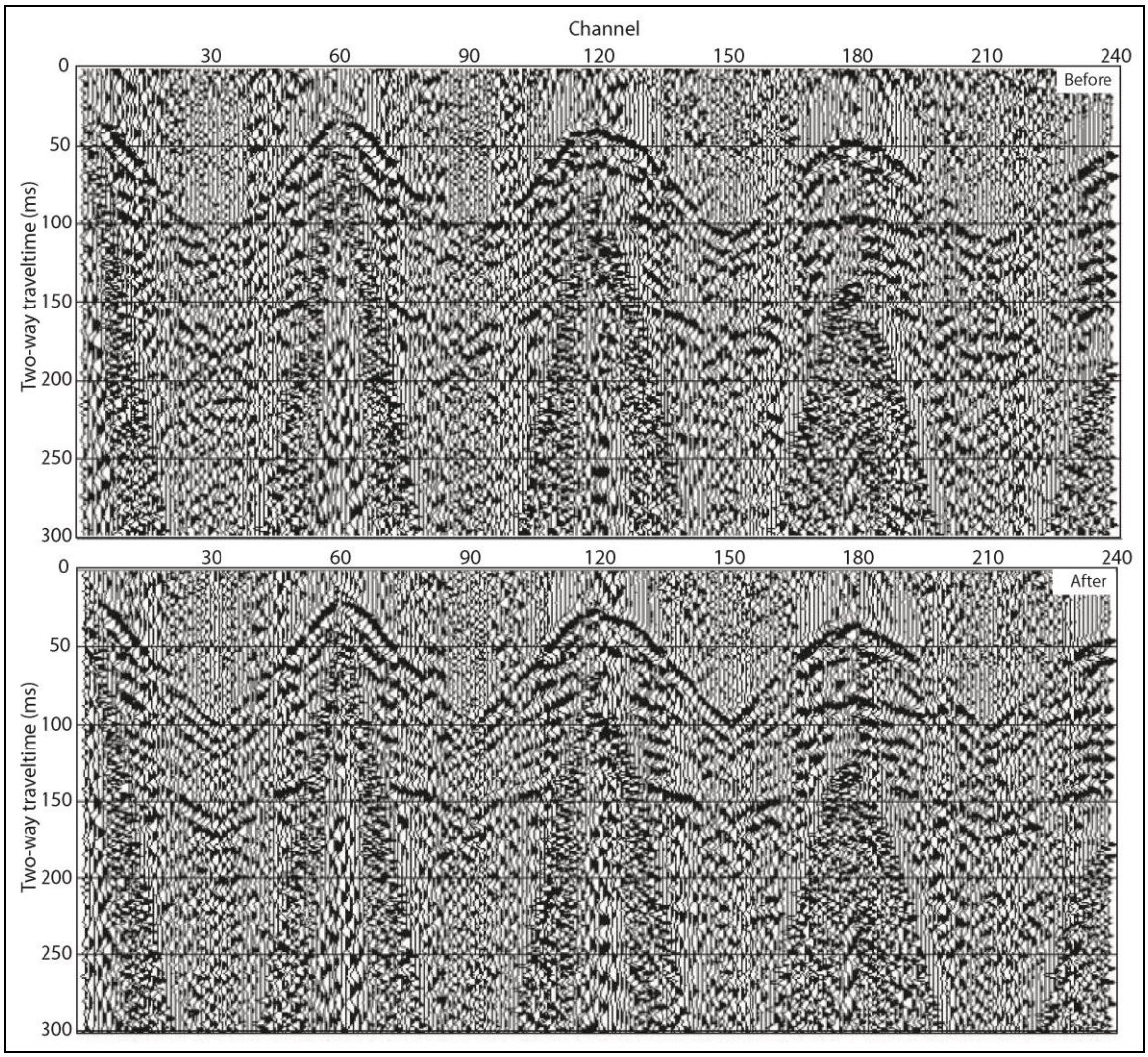

Figure 6, Hess

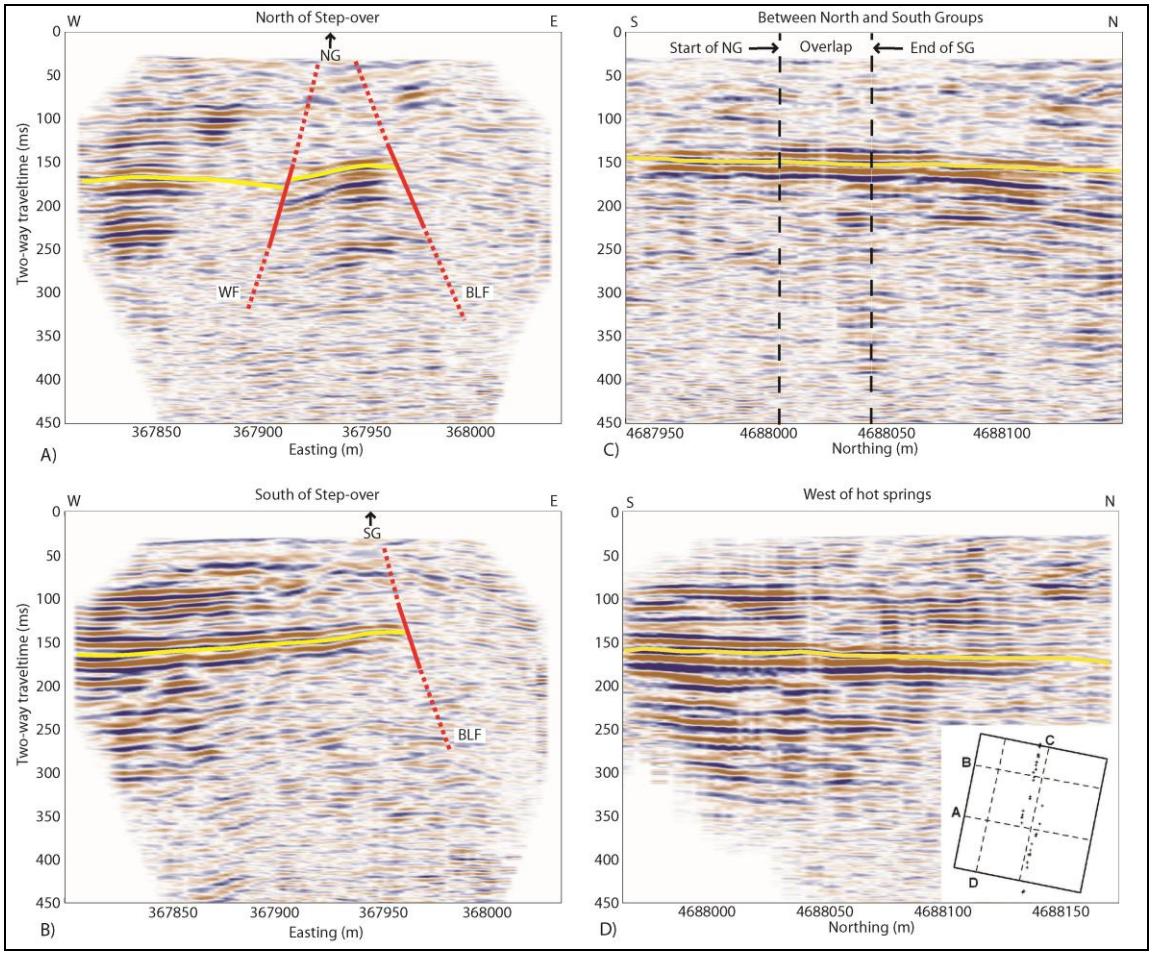

Figure 7, Hess

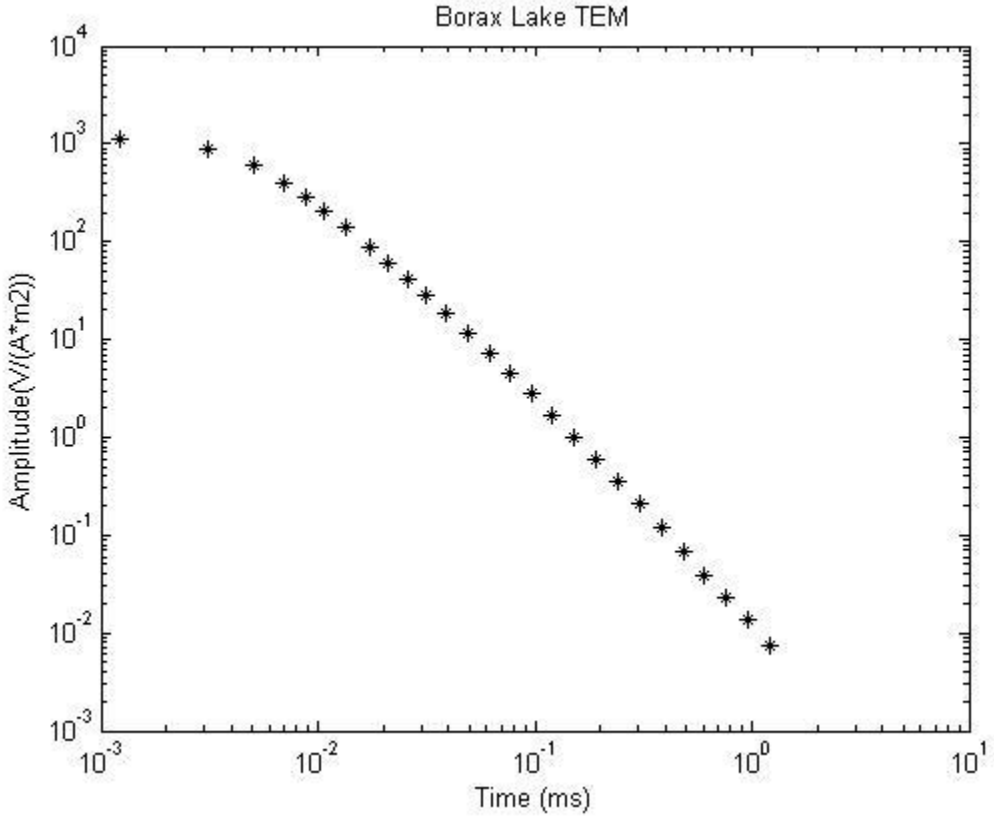

Figure 8. Hess

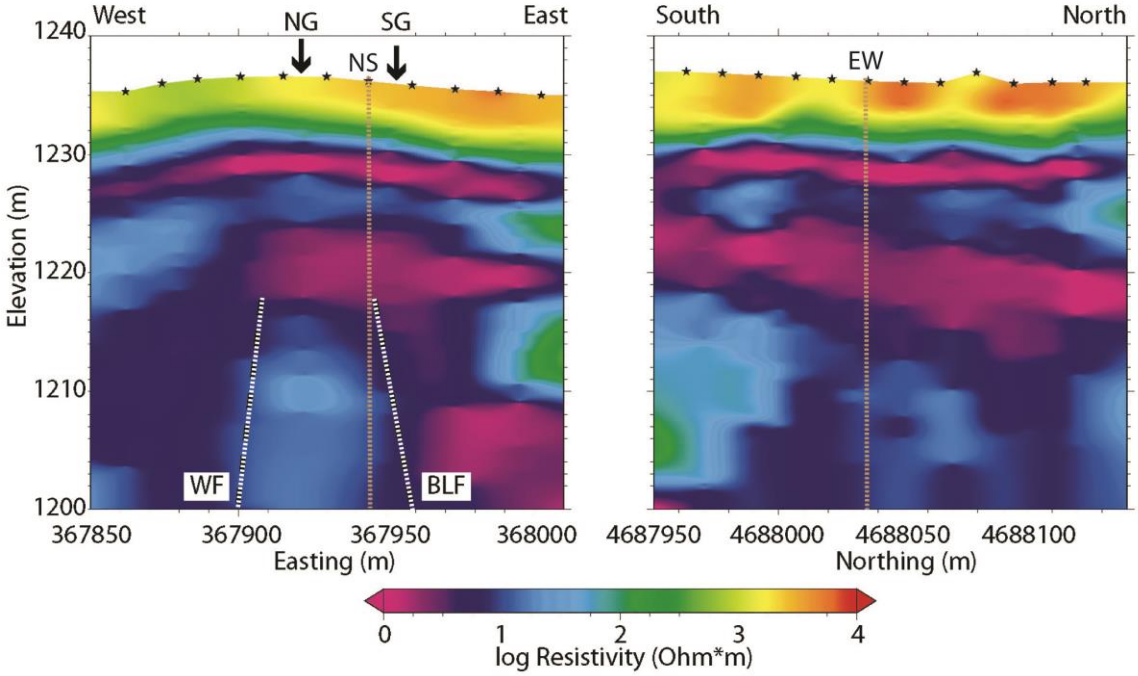

Figure 9. Hess

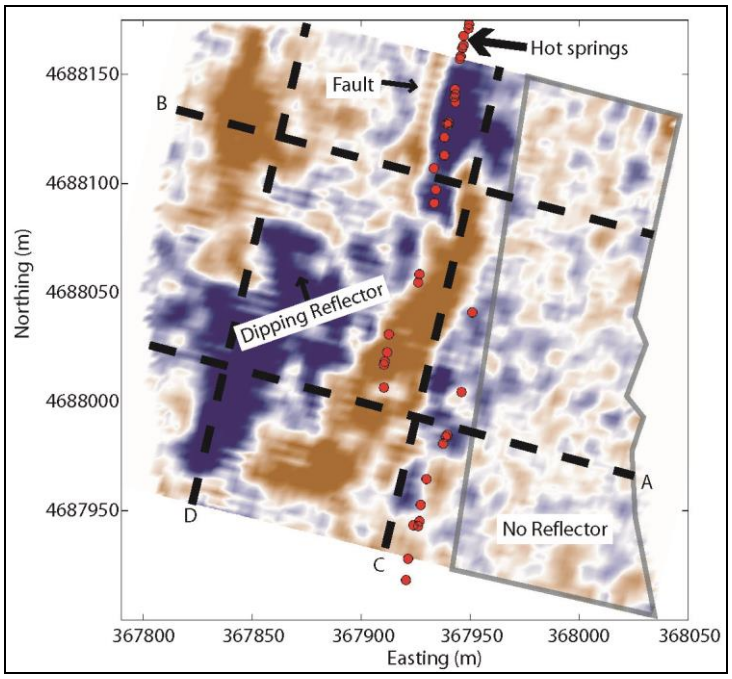

Figure 10. Hess

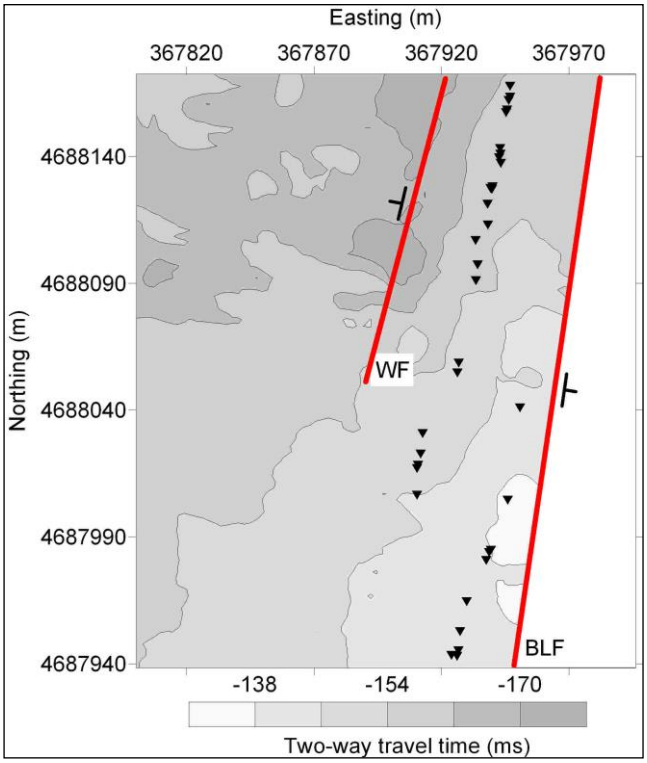

Figure 11, Hess

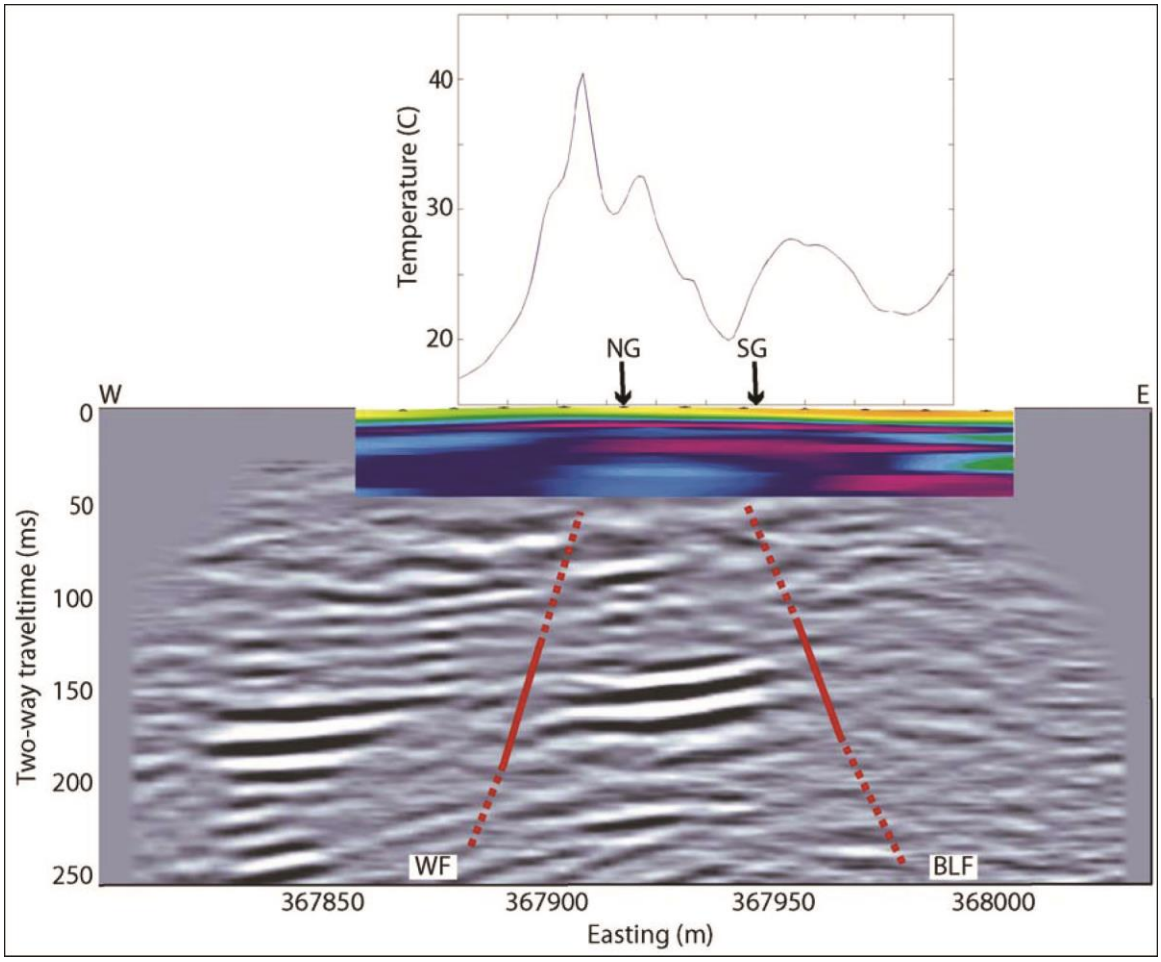

Figure 12, Hess